Highly Distorted Platinum Nanorods for High-Efficiency Fuel Cell Catalysis

Lingzheng Bu[1], Bolong Huang[2], Yiming Zhu[1], Fandi Ning[3], Xiaochun Zhou[3] & Xiaoqing Huang[1]*

[1]College of Chemistry, Chemical Engineering and Materials Science, Soochow University, Jiangsu 215123 (China), [2]Department of Applied Biology and Chemical Technology, Hong Kong Polytechnic University, Hung Hom, Kowloon, Hong Kong SAR (China), [3]Division of Advanced Nanomaterials, Suzhou Institute of Nano-Tech and Nano-Bionics, Chinese Academy of Sciences (CAS), Jiangsu 215123 (China)

*Corresponding author: hxq006@suda.edu.cn

Different from studies where less defective platinum (Pt)-based nanomaterials have been widely used to improve the catalysis of the oxygen reduction reaction (ORR) for proton-exchange membrane fuel cells (PEMFCs), herein we have demonstrated that a new class of Pt nanorods (NRs) with a highly distorted configuration can be applied as an advanced, high-efficiency fuel cell catalyst, as transformed from spongy Pt–tellurium NRs ($PtTe_2$ NRs) through sequential chemical and electrochemical aging procedures. The resulting highly distorted Pt NRs exhibit excellent ORR-specific and mass activities of 4.70 mA cm^{-2} and 2.77 A mg^{-1}_{Pt} at 0.90 V versus the reversible hydrogen electrode (RHE), which are 18.8 and 16.3 times higher than those of commercial Pt/C catalyst, and the mass activity is 6.3 times higher than 2020 U.S. Department of Energy target. Additionally, negligible activity decays were observed after 30,000 cycles. The high ORR performance endows these unique Pt NRs with enhanced activity and lifetimes for practical fuel cell catalysis in comparison with commercial Pt/C, which is consistent with the experimental results. It has been demonstrated that the anomaly of strong electron–lattice coupling suppresses Coulombic repulsion for barrier-free electron transfer while concurrently exposing a large number of active sites, which is a key to superior high-performance fuel cell reactions.
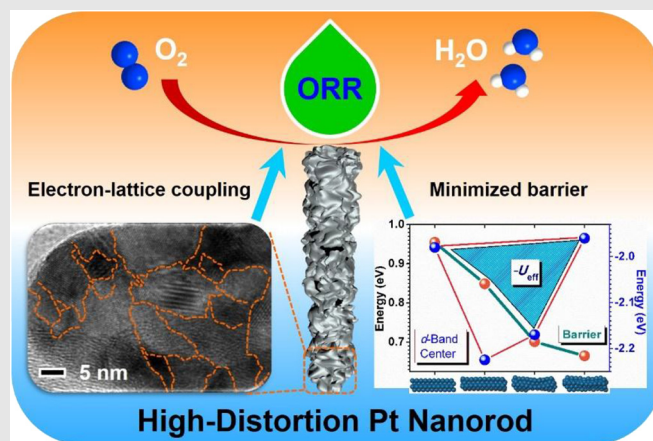
Keywords: distortion, oxygen reduction reaction, platinum, nanorod, fuel cell catalysis

Introduction

The proton-exchange membrane fuel cell (PEMFC), as one of the most promising energy conversion devices, has recently drawn considerable attention due to advantages such as convenience, cleanliness, ample fuel sources, low working temperature, and high energy density.[1–5] Practically, PEMFCs confront the activity, durability, and selectivity of applied catalysts issues, in which the performances of cathodic catalysts play a decisive role in the performance of the device.[6,7] Platinum (Pt)-based nanocrystals (NCs) are the most efficient catalysts for cathodic oxygen reduction reactions (ORR) in the PEMFC.[8–12] However, poor utilization rates lead to

the high cost of Pt, which impedes their practical applications,[13–16] although tremendous efforts have been spent on developing highly efficient Pt-based alloys with well-controlled nanostructures reduce cost and improve performance.[17–19] Among various effective strategies, the precise surface/interface tuning of the interaction between catalysts and reactants is believed to be the decisive step in maximizing the targeted electrocatalysis.[20–24] Accordingly, the well-controlled Pt–skin surface is designed for Pt-based alloys, leading to higher performance for fuel cell reactions.[25] However, the poor cycling stability under operating conditions prevents these types of materials from occupying an appreciable market share. In fact, the structural defects located in the highly polycrystalline Pt-based nanomaterials can provide a workable platform to realize high Pt utilization through numerous active step atoms in place of the defects. The disordered structure configuration caused by the polycrystalline feature commonly brings about the introduction of high surface strain, which has become one of the most significant improvement factors to optimize fuel cell catalysis,[26,27] especially for bimetallic Pt-based NCs with high transition metal content. Thus, exploring unique Pt-based nanomaterials with high surface distortion for boosting fuel cell catalysis is an urgent and formidable challenge.

One-dimensional (1D) nanostructures are ideal nanostructures owing to their high aspect ratio and important ability to engineer surface distortion along the longitudinal direction of nanowires (NWs) or nanorods (NRs). Therefore, achieving fine distortion control in 1D nanostructures leads to the successful creation of high-performance catalysts.

Herein, we report a new class of Pt NRs with a highly distorted configuration for simultaneously boosting ORR and the overall fuel cell reaction. The highly distorted Pt NRs originate from initially synthesized Pt–tellurium NRs (PtTe$_2$ NRs) through a series of sequential chemical and electrochemical aging processes. The resulting highly distorted Pt NRs (H-Pt NRs) exhibit superior ORR performance in comparison to weakly distorted Pt NRs (W-Pt NRs) and commercial Pt/C. To be specific, the H-Pt NRs deliver enhanced specific and mass activities for ORR that are 18.8 and 16.3 times higher than those of commercial Pt/C and 4.6 and 5.7 times greater than those of W-Pt NRs, respectively. The H-Pt NRs are also stable under strong acidic ORR medium with negligible activity decay after 30,000 potential cycles, along with a largely maintained distorted structure after a long-term stability test. We reveal that vast short-range disordering renders a high Pt-5d electronic affinity with negative correlation. The electron-rich characteristics, an anomaly for these types of materials, critically elevate ORR efficiency to overcome on-site electron-transfer barriers. The H-Pt NRs also exhibit much higher activity and lifetime for the overall fuel cell, in comparison with commercial Pt/C, paving a pathway for new classes of fuel cell electrocatalysts.

Experimental Methods

Preparation of spongy PtTe$_2$ NRs

In the preparation of PtTe$_2$ NRs, 10 mg platinum (II) acetylacetonate (Pt(acac)$_2$), 12.8 mg potassium tellurite (K$_2$TeO$_3$), 35.6 mg L-ascorbic acid (AA), 100 mg polyvinylpyrrolidone (PVP), 5 mL water, and 5 mL ethylene glycol (EG) were added into a vial (volume: 35 mL). After the vial had been capped, the mixture was ultrasonicated for around 1 h. The resulting mixture was transferred to a Teflon-lined stainless-steel autoclave and then heated at 180 °C for 5 h in an oven, before it was cooled to room temperature. The resulting products were collected by centrifugation and washed with an ethanol/acetone (v/v 1:9) mixture.

Preparation of the MEA for fuel cell catalysis

The membrane electrode assembly (MEA) with an active area of 1 cm^2 was prepared and used in this study as follows. The catalyst layer was spread on the composite electrode by screen printing. The catalyst ink was prepared by dropping Nafion perfluorinated resin solution (5 wt% in lower aliphatic alcohols and water) into mixed solution of deionized water and isopropanol (v/v 1:1) and with 14.1% H-Pt NRs/C or 20% Pt/C catalyst in an ultrasonic bath for 30 min. The Nafion content was 40% in the 20% Pt/C ink. While we set a series of values of Nafion in the H-Pt NRs/C ink to discover the optimal content of Nafion, the optimized content of Nafion was 42% in the 14.1% H-Pt NRs/C ink. The cathode catalyst loading was 0.5 mg$_{Pt}$ cm^{-2} for the MEA with Pt/C and 0.35 mg$_{Pt}$ cm^{-2} for the MEA with H-Pt NRs/C, while the Pt loading was 0.5 mg$_{Pt}$ cm^{-2} for the anode (70% Pt/C, 20% Nafion). After coating the catalyst to the electrode, the electrode was placed in baking oven for 2 h at 105 °C. The thickness of the carbon electrode was 190 μm and 20% water-resistant, which was purchased from Toray. Then, a Nafion 211 (25 μm) membrane was hot-pressed with two electrodes at a pressure of 40 kg$_f$ cm^{-2} and temperature of 130 °C for 2 min.

The electrochemical performance was measured by an electrochemical workstation (CS). The test mode was linear sweep voltammetry with a sweep rate of 2 mV s^{-1} and cutoff voltage of 0.2 V. During the test, the cathode of the fuel cell is used as the working electrode, and the anode is used as the counter electrode and reference electrode. The test temperature of the self-breathing fuel cell is 25 °C. Specifically, one side of the anode is actively supplied with hydrogen, the other side of the cathode is directly exposed to the air, which is passively supplied. The experiments were performed with pure hydrogen at room temperature and atmospheric pressure. The pure

hydrogen is prepared from a hydrogen generator. The flow rate of hydrogen is 15 mL min^{-1}. The polarization curve of the fuel cell is measured by linear scanning at a rate of 2 mV s^{-1}. The fuel cell life test is set to a constant current discharge of 50 mA cm^{-2}.

DFT models and calculations

We carried out the density functional theory (DFT) + U calculations using CASTEP code by the rotationally invariant Hubbard-U theory.[28,29] The Hubbard-U parameter has been consistently determined for pseudized Pt-5d by our linear response method for U determination.[30-35] The geometric optimization uses the Broyden–Fletcher–Goldfarb–Shanno (BFGS) algorithm for all calculations. The Perdew-Burke-Ernzerhof (PBE) function was chosen for PBE + U calculations with a plane-wave basis set cutoff energy of 750 eV. The ensemble DFT (EDFT) method is used to improve convergence of a d-orbital transition-metal-based system.[36]

For the twisted Pt model, a multifaceted cleaved Pt structure within a large vacuum environment has been built with160 atoms and a radial vacuum separation of 15 Å. All atoms were fully varied flexibly through the BFGS geometry relaxation process. Model 0 is the non-twisted structure with all Pt sites frozen, and models 1–3 were built based on model 0 being gradually twisted with different angles from different regions. The amorphization was finally determined using the simulated radial distribution function (RDF).

For the Monkhorst–Pack k-point sampling, the reciprocal space integration was performed using a mesh of $2 \times 2 \times 1$ with Gamma center-off, which has been self-consistently selected for total energy minimization.[37] With these special k-points, the total energy converges to less than 5.0×10^{-7} eV per atom. The Hellmann–Feynman forces on the atom converged to less than 0.001 eV Å^{-1}.

The Pt, O, and H norm-conserving pseudopotentials were generated using the OPIUM code in the Kleinman–Bylander projector form,[38] and the nonlinear partial core correction and a scalar relativistic averaging scheme were used to treat the Pt spin–orbital coupling effect.[39,40] We chose the (5d, 6s, 6p), (2s, 2p), and (1s) states as the valence states of Pt, O, and H atoms, respectively. The Rappe Rabe Kaxiras Joannopoulos (RRKJ) method was chosen for pseudopotential optimization.[41] The Hubbard-U parameter has been self-consistently determined based on our previously developed method.[42] For electronic state calculations, we used the self-consistent determination for the U correction on the localized 5d orbitals to correct the on-site Coulombic energy of the electron spurious self-energy. By that method, the Hubbard-U parameters on the near-fully occupied shells of 5d^9 orbitals of Pt were self-consistently determined to be U$_d$ = 6.91 eV, as averaged by the four different models.

Results and Discussion

Synthesis and characterization of spongy PtTe$_2$ NRs

The spongy PtTe$_2$ NRs in were first synthesized in aqueous media (details in the "Experimental Methods" section) and the morphology was analyzed by high-angle annular dark-field scanning transmission electron microscopy (HAADF-STEM). Highly monodisperse NRs were the dominant products with yields approaching 100% (Figures 1a and 1b; Supporting Information Figures S1a–c). The average diameter was 32.2 nm and the average length reaches 147.0 nm with an average aspect ratio of 4.6 (Supporting Information Figures S1d and e). The PtTe$_2$ NRs were highly spongy with uneven surfaces, as revealed by the magnified HAADF-STEM images (Figure 1b; Supporting Information Figure S1c). TEM energy-dispersive X-ray spectroscopy (TEM-EDS) shows that the overall composition ratio of Pt/Te is 33.8/66.2, which is very close to the inductively coupled plasma atomic emission spectroscopy (ICP-AES) (33.5/66.5) and scanning electron microscopy EDS (33.4/66.6) results (Figure 1c; Supporting Information Figure S1f). The crystal phase of the spongy PtTe$_2$ NRs was characterized by powder X-ray diffraction (PXRD) (Figure 1d), showing a trigonal phase (P-3m1 (164), JCPDS no. 88-2277). The PtTe$_2$ NRs exhibit obvious polycrystalline nature, as revealed by the selected-area electron diffraction (SAED) pattern and the fast Fourier transform (FFT) pattern (Figures 1e–g and inset in Figure 1g). High-resolution TEM (HRTEM) images of a single PtTe$_2$ NR clearly demonstrate their highly porous features (Figure 1g; Supporting Information Figures S2b–d). Due to the sponginess, the lattice fringes of PtTe$_2$ NRs were not continuous throughout the whole NR. The displayed interplanar spacing of 0.290 nm corresponds to the (011) facet of alloyed PtTe$_2$ nanostructure with a hexagonal phase (P-3m1 (164)) (Figure 1g), which is consistent with the PXRD results (Figure 1d). The HAADF-STEM-EDS elemental mapping technique was used to characterize the elemental distributions of Pt and Te on the PtTe$_2$ NRs, where the Pt (green), Te (red), and combined (green vs red) images (Figure 1h) along with the corresponding line-scan results (Figure 1h$_1$,h$_2$) confirm even Pt and Te distributions throughout the whole PtTe$_2$ NRs. Based on the aforementioned HAADF-STEM, EDS, PXRD, HRTEM, HAADF-STEM-EDS elemental mapping, and line-scan results, it can be concluded that the unique 1D PtTe$_2$ NRs with spongy features have been successfully synthesized.

Coupled chemical and electrochemical strategy to construct H-Pt NRs/C

To obtain high-performance electrocatalysts, a series of chemical and electrochemical techniques were used to
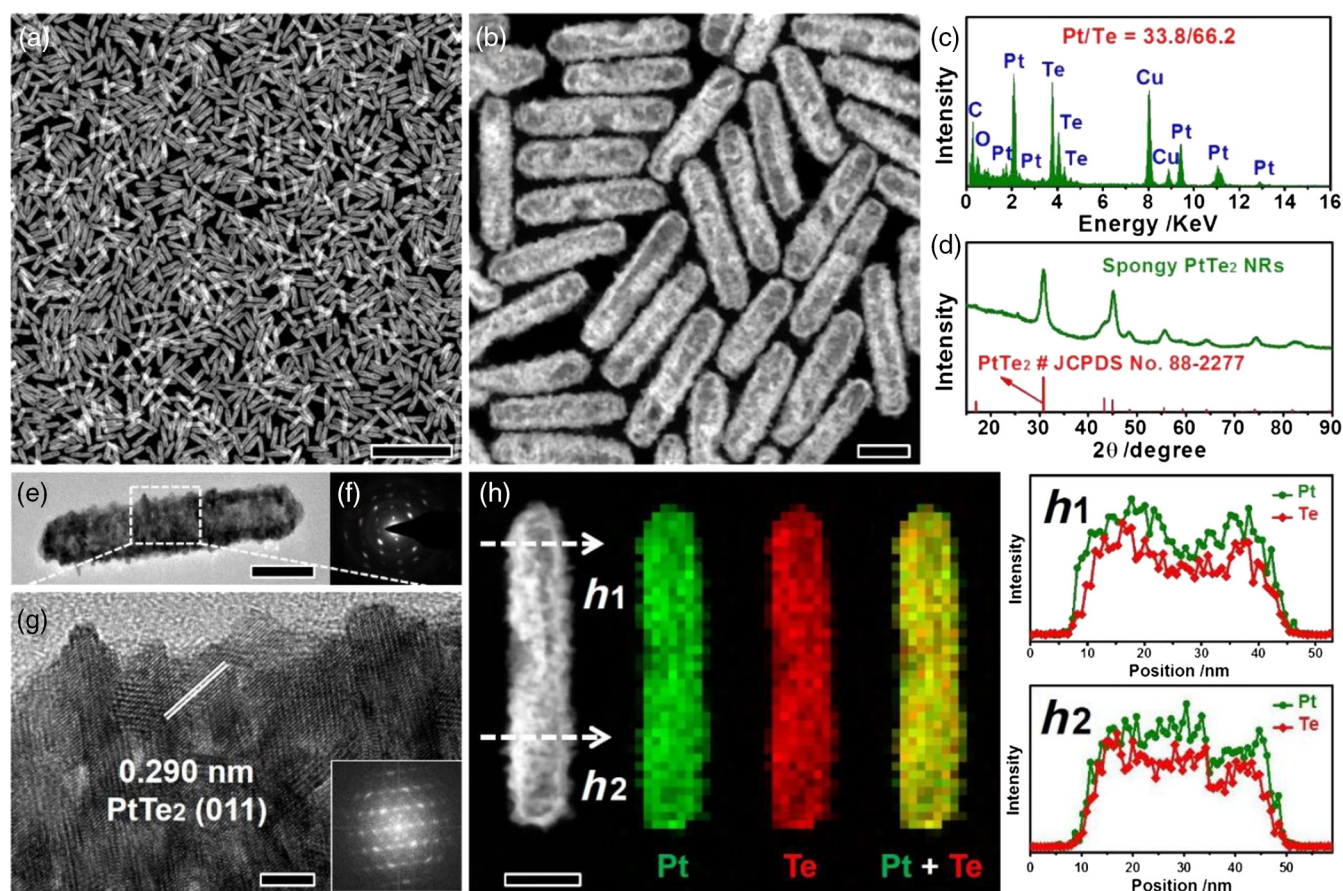
Figure 1 | *Morphology and structure characterizations of spongy PtTe₂ NRs. (a and b) HAADF-STEM images, (c) TEM-EDS, and (d) PXRD pattern of the PtTe₂ NRs. (e) TEM image, (f) SAED pattern, and (g) HRTEM image of the PtTe₂ NR. The inset in (g) is the corresponding FFT pattern. (h) HAADF-STEM image and elemental mappings as well as (h₁, h₂) line scans of the PtTe₂ NR. Pt in green, Te in red, and integration of Pt and Te. The composition ratio of Pt/Te is 33.5/66.5, as revealed by ICP-AES. The scale bars in (a), (b), (e), (g), and (h) are 500, 50, 40, 5, and 40 nm, respectively.*

handle the spongy PtTe₂ NRs, and the corresponding evolutionary processes of structure, composition, and crystal phase in the different stages were investigated in detail (Figure 2; Supporting Information Figures S3–S9). These PtTe₂ NRs were first loaded on carbon powder to prepare the PtTe₂ NRs/C, where the morphology, composition, and crystal phase were largely maintained, as revealed by the TEM, EDS, and PXRD results (Figure 1; Supporting Information Figure S3). After washing with acetic acid, the PtTe₂ NRs/C showed limited structural changes (Figures 2a–c; Supporting Information Figures S4 and S5). After further annealing at 250 °C in atmosphere for 1 h, the structure of the PtTe₂ NRs/C changed sequentially (Figures 2d–f; Supporting Information Figures S6 and S7), where the NR shape and elemental distribution can be maintained (Figures 2d–f; Supporting Information Figure S7a), while the overall composition of Pt/Te showed observable changes (from 39.4/60.6 to 49.5/50.5; Supporting Information Figures S4a and S6a). As shown in Supporting

Information Figure 6b, a new crystal phase matching well with the face-centered cubic (fcc) Pt phase (JCPDS no. 04-0802) was observed, which shows that the PtTe NRs/C with trigonal PtTe₂ and cubic Pt phases have been obtained from the initially prepared PtTe₂ NRs through the sequential chemical aging processes (Supporting Information Figures S6 and S7).

After chemical aging, electrochemical aging was then carried out for enhanced fuel cell catalysis, as the electrochemical dealloying process usually results in the leaching of transition metals and thus numerous defects and strong lattice strain (beneficial for producing high surface distortion). We can see that the PtTe NRs/C, after further electrochemical aging, showed large differences in composition, crystal phase, and surface distortion compared with those of the PtTe₂ NRs/C not electrochemically aged. We further characterized the PtTe₂ NRs/C after both chemical and electrochemical aging in detail (Figures 2g–j; Supporting Information Figures S8 and S9). Compared with the chemically aged PtTe
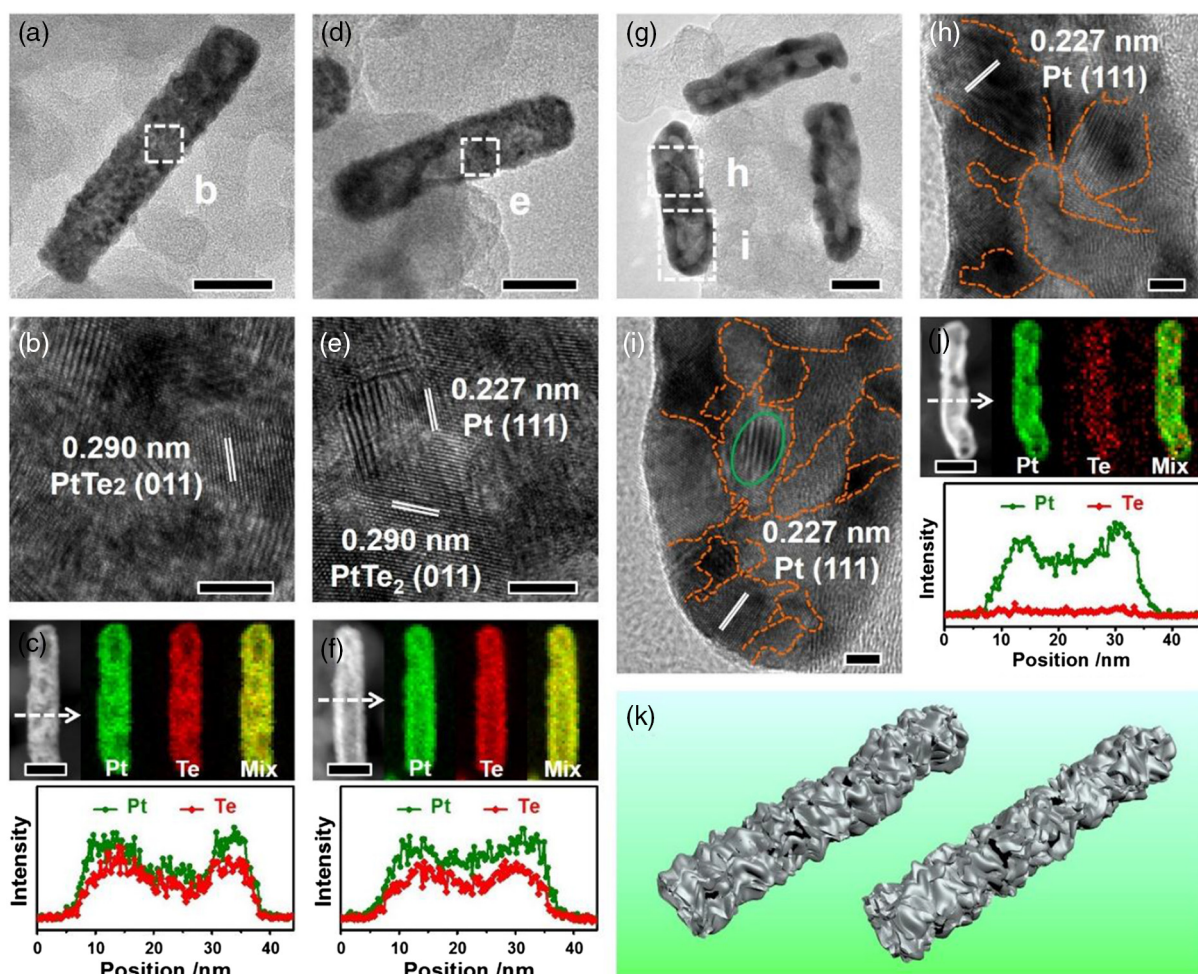
Figure 2 | *Structure and composition characterizations of spongy PtTe$_2$ NRs/C after different evolution processes. (a, d, and g) TEM images, (b, e, h, and i) HRTEM images, (c, f, and j) HAADF-STEM images, and elemental mappings and corresponding line scans of the PtTe$_2$ NRs/C in different stages: (a–c) after washing with acetic acid twice, (d–f) after washing with acetic acid twice and further annealing at 250 °C in the atmosphere for 1 h, (g–j) after chemical aging and then the electrochemical aging in 0.1 M HClO$_4$ solution for 2000 CV cycles. (k) The corresponding 3D models of the resulting highly distorted Pt NRs. The scale bars in (a), (c), (d), (f), (g), and (j) are 40 nm. The scale bars in (b), (e), (h), and (i) are 5 nm.*

NRs/C, the 1D morphology of the chemically/electrochemically aged PtTe$_2$ NRs/C can be largely maintained (Supporting Information Figures S7a and S9a), while the overall composition ratio of Pt/Te changed from 49.5/50.5 to 96.2/3.8 (Supporting Information Figures S6a and S8a). HRTEM and PXRD results jointly reveal the complete crystal phase transformation from the trigonal PtTe$_2$ phase to the cubic Pt phase (Figures 2h and 2i; Supporting Information Figures S3d, S8b, and S9b–d). We further studied the structure of the resultant Pt NRs/C by HRTEM in detail. The discontinuous lattice fringes and numerous lattice mismatches can be obviously observed around the Pt NRs/C (Figures 2h and 2i; Supporting Information Figures S9b–d), which are derived from the polycrystalline nature of the Pt NRs. The discontinuities of lattice fringes can create many irregular

facet boundaries (the orange dotted lines labeled in Figures 2h and 2i), while the lattice mismatches result in the presence of a large number of step atoms. These jointly construct the unique nanostructure of the Pt NRs with numerous defects. Further, the structurally disordered configuration associated with the abundant defects can largely improve the global strain effect (as the area highlighted with a green ellipse in Figure 2i). Consequently, the potentially strong surface boundary effect, large defect effect, and high global strain collectively contribute to the extensive distortion of the Pt NRs/C. The combined results of HRTEM, elemental mapping, and corresponding line scans confirm the successful creation of highly distorted Pt NRs/C (namely H-Pt NRs/C) (Figures 2h–j; Supporting Information Figure S9b–g). The corresponding 3D models of the H-Pt NRs
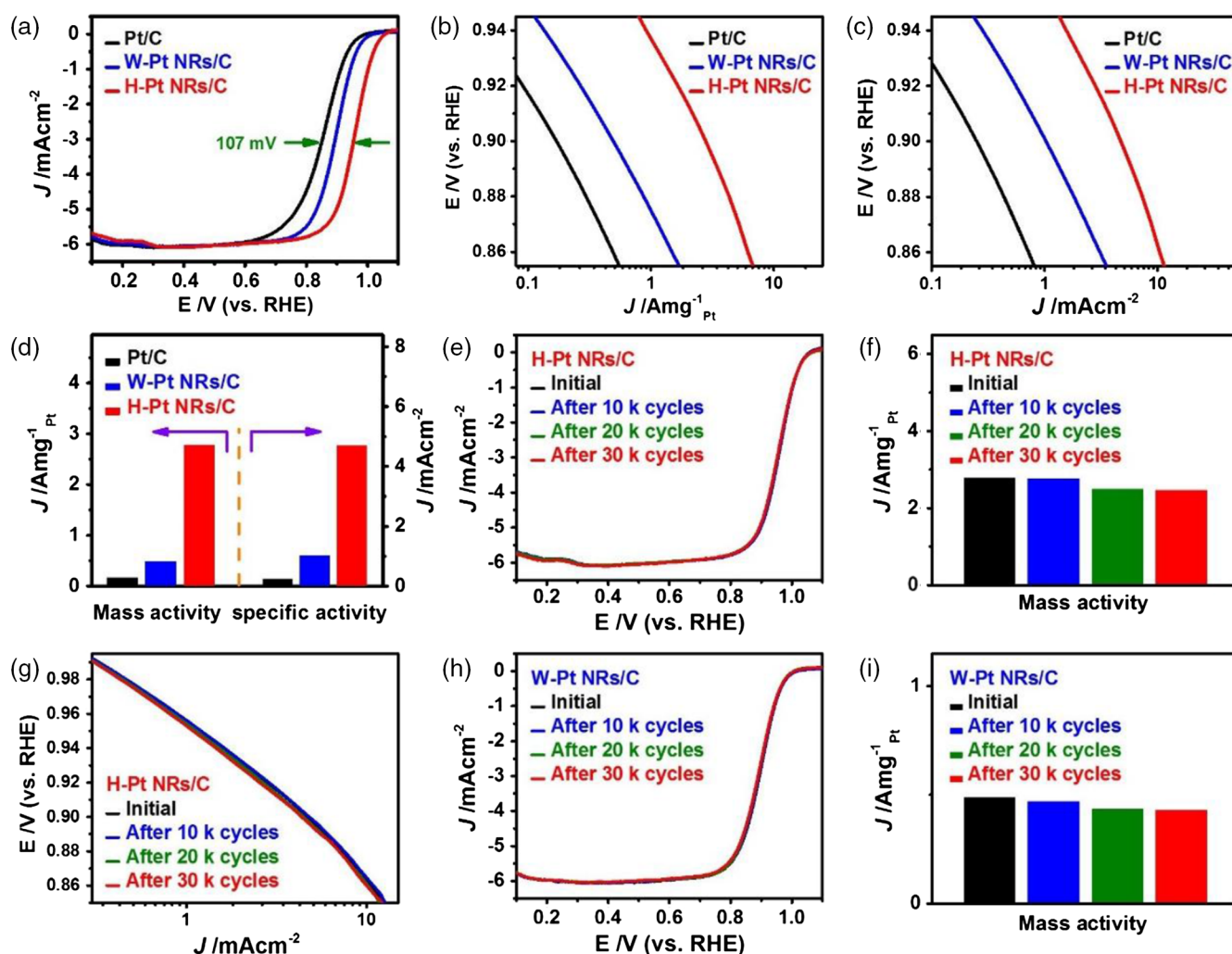
Figure 3 | *Electrocatalytic performances of H-Pt NRs/C, W-Pt NRs/C, and commercial Pt/C for ORR. (a) ORR polarization curves of different catalysts. The ORR polarization curves were recorded at room temperature in O_2 -saturated 0.1 M $HClO_4$ aqueous solution after Ohmic drop correction. The scan rate and rotation rate for ORR measurements were 10 mV s^{-1} and 1600 rpm, respectively. (b and c) ORR mass activity and specific activity Tafel plots of different catalysts. (d) Histogram of mass and specific activities of different catalysts for ORR at 0.90 V versus RHE. (e) ORR polarization curves of the H-Pt NRs/C before and after different potential cycles between 0.6 and 1.1 V versus RHE. (f) The changes on mass activities of the H-Pt NRs/C before and after different potential cycles. (g) ORR-specific activity Tafel plots of the H-Pt NRs/C before and after different potential cycles. (h) ORR polarization curves of the W-Pt NRs/C before and after different potential cycles between 0.6 and 1.1 V versus RHE. (i) The changes on mass activities of the W-Pt NRs/C before and after different potential cycles.*

are shown in Figure 2k for better understanding of this unique nanostructure. Considering the combination of unique 1D nanostructure and maximized distortion configuration, the H-Pt NRs/C materials are expected to possess superior fuel cell performance.

ORR performance of obtained H-Pt NRs/C

The electrochemical performance of the resulting H-Pt NRs/C was systematically studied and benchmarked against the commercial Pt/C from Johnson Matthey (Pt/C, 20 wt % Pt on Vulcan XC72R carbon, Pt particle

size: 2–5 nm; Supporting Information Figures S10a and b) and the weakly distorted Pt NRs/C (namely W-Pt NRs/C; Supporting Information Figure S11). Supporting Information Figure S12 shows the typical cyclic voltammograms (CVs) of H-Pt NRs/C, W-Pt NRs/C, and commercial Pt/C in N_2-purged 0.1 M $HClO_4$ solution at a sweep rate of 50 mV s^{-1}. The electrochemical active surface area (ECSA) was calculated according to the CV curves, where the ECSAs for H-Pt NRs/C, W-Pt NRs/C, and commercial Pt/C were determined to be 59.0, 48.1, and 68.2 m^2 g^{-1}, respectively (Supporting Information Table S1).

The cathodic ORR was first used as the model reaction to evaluate the performances of different electrocatalysts. Figure 3a shows the ORR polarization curves of H-Pt NRs/C, W-Pt NRs/C, and commercial Pt/C carried out in O_2-saturated 0.1 M $HClO_4$ solution under an Ohmic drop correction. The half-wave potential for the H-Pt NRs/C was at 0.955 V, which is much higher than those of the W-Pt NRs/C (0.891 V) and the commercial Pt/C (0.848 V), revealing the superior ORR activity of the H-Pt NRs/C. The mass activity and specific activity Tafel plots for different catalysts also demonstrate the highest ORR activity of the H-Pt NRs/C (Figures 3b and 3c). As shown in Figure 3d and Supporting Information Table S1, the specific activity of H-Pt NRs/C can reach up to 4.70 mA cm^{-2} at 0.90 V versus RHE, 4.6- and 18.8-fold higher than those of the W-Pt NRs/C (1.02 mA cm^{-2}) and the commercial Pt/C (0.25 mA cm^{-2}). The H-Pt NRs/C also displays the highest mass activity of 2.77 A mg^{-1}_{Pt} at 0.90 V versus RHE, which is 5.7 and 16.3 times greater than those of the W-Pt NRs/C (0.49 A mg^{-1}_{Pt}) and commercial Pt/C (0.17 A mg^{-1}_{Pt}) (Figure 3d; Supporting Information Table S1), respectively, and the mass activity is ~6.3 times that of the 2020 U.S. Department of Energy (DOE) target (0.44 A mg^{-1}_{Pt}),[43] demonstrating that the H-Pt NRs/C is one of the most efficient Pt-based ORR electrocatalysts reported to date (Supporting Information Table S2).

Accelerated durability tests (ADTs) were performed to evaluate the ORR durability of these catalysts. Figures 3e and 3f and Supporting Information Figures S13a and b show the CVs and corresponding polarization curves of the H-Pt NRs/C before and after 10,000, 20,000, and 30,000 potential cycles. After 30,000 sweeping cycles of ADTs, the ECSA of H-Pt NRs/C changed from 59.0 to 57.0 m^2 g^{-1} (3.4% loss; Supporting Information Figures S13a and b) with only 10.8% mass activity loss (Figures 3e and 3f). The small changes in mass activity and specific activity Tafel plots for the H-Pt NRs/C also suggest its excellent ORR stability (Figure 3g; Supporting Information Figure S14a). However, the W-Pt NRs/C shows more changes in CV and negative shift in ORR polarization curves under the same conditions with 12.0% enhancement in ECSA and 12.3% loss in mass activity (Figures 3h and 3i; Supporting Information Figures S13c and d). By sharp contrast, the commercial Pt/C shows much larger negative shifts in ORR polarization curves with 48.5% loss of mass activity (Supporting Information Figures S14b and c), along with 55.9% ECSA loss (Supporting Information Figures S13e and f). Moreover, after 30,000 CV cycles of ADTS, the H-Pt NRs/C, W-Pt NRs/C, and commercial Pt/C were studied by TEM, EDS, HRTEM, elemental mappings, and line scans (Supporting Information Figures S10c and d, and S15 and S16). It was found that the distorted configuration and spongy structure of H-Pt NRs/C can be largely maintained after long-term ORR stability measurement (Supporting Information Figures S8, S9, and S15), while the W-Pt NRs/C showed larger change in its spongy structure after 30,000 potential cycles of ADTs (Supporting Information Figures S11 and S16). In addition, the commercial Pt/C exhibited obvious size change and serious aggregation after the ORR stability test (Supporting Information Figures S10c and d). All these results clearly demonstrate that the H-Pt NRs/C is very active and durable for cathodic ORR.

MEA performance evaluation for obtained H-Pt NRs/C

To further demonstrate the superior structure advantage of H-Pt NRs/C compared with commercial Pt/C, we also evaluated the fuel cell performances of H-Pt NRs/C and Pt/C in single H_2–air self-breathing fuel cells. Figure 4a shows the voltage–current (V–I) polarization curves and power density distributions measured under ambient temperature and pressure conditions with a cathode Pt loading of 0.35 mg_{Pt} cm^{-2} for H-Pt NRs/C and 0.50 mg_{Pt} cm^{-2} for Pt/C. According to the V–I polarization curves, the open-circuit voltage (OCV) of H-Pt NRs/C for MEAs was measured to be 0.994 V versus RHE, higher than that of Pt/C for MEA (0.902 V vs RHE). Simultaneously, the peak power densities of H-Pt NRs/C and Pt/C for MEA were determined to be 120 m and 78.8 mW cm^{-2}, respectively. As shown in Figure 4b, the normalized peak power density of H-Pt NRs/C for MEA can reach up to 342.9 mW mg^{-1}_{Pt}, 2.2 times larger than that of Pt/C for MEA (157.6 mW mg^{-1}_{Pt}), revealing superior fuel cell activity of H-Pt NRs/C in single H_2–air fuel cell.

Furthermore, we also evaluated the catalytic durability of the H-Pt NRs/C in the fuel cell and benchmarked against commercial Pt/C. After 72 h of constant current discharge at 50 mA cm^{-2} (Figure 4c), the voltage showed only an 89 mV decay for the H-Pt NRs/C (13.4% loss, Figure 4d), while Pt/C exhibited as high as 346 mV voltage loss (50.1% loss, Figure 4d), demonstrating the superior catalytic stability of H-Pt NRs/C in an H_2–air fuel cell. Hence, these unique H-Pt NRs have better performances than commercial Pt for ORR and the overall fuel cell.

DFT and experimental origins of performance improvement

To shed light on the much enhanced ORR performance of the H-Pt NRs/C compared with W-Pt NRs/C and commercial Pt/C, we investigated the excellent ORR performance with DFT calculations. Regarding electronic character on catalytic reactivity, shape- or site-dependent factors have been considered. Here, the projected partial density of states (PDOSs) shows the site-dependent 5d-band variations based on distortions. With the distortion degree increased, the dominant peak (at E_V–1 eV, i.e., E_V = 0 for Fermi level, E_F) gradually
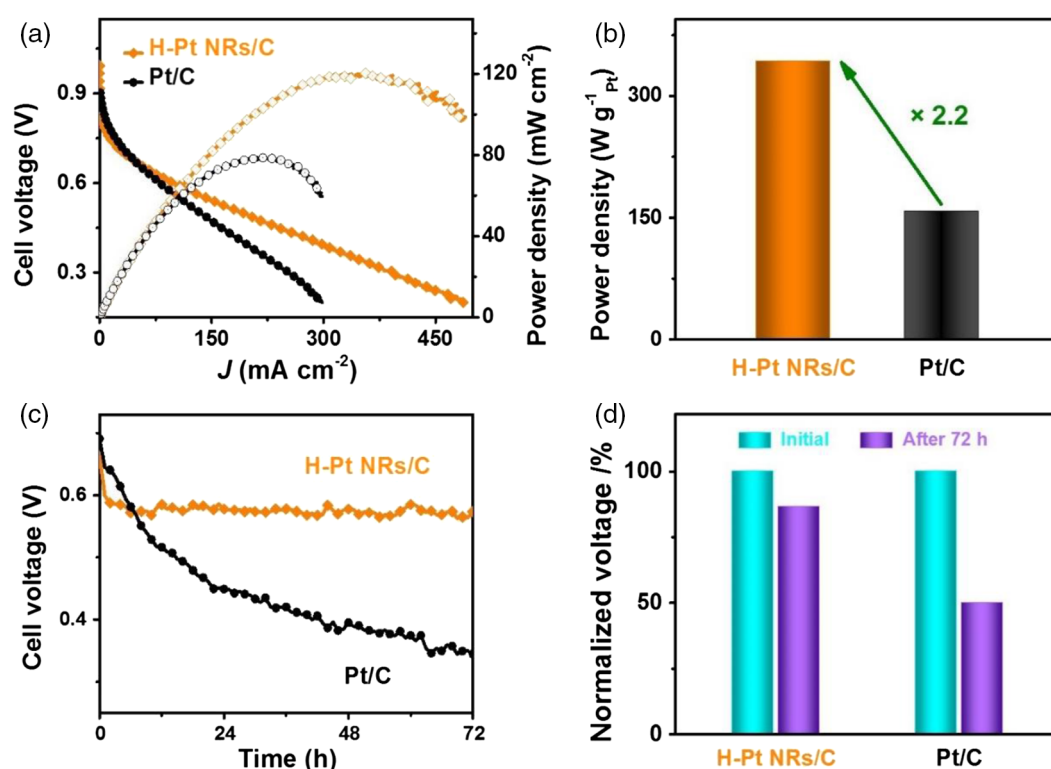
Figure 4 | *MEA performance evaluation of H-Pt NRs/C in the fuel cell. (a) H_2–air fuel cell V–I polarization and power density curves for H-Pt NRs/C and commercial Pt/C. (b) Histogram of power densities via normalization with respect to the mass loading of Pt for different catalysts. (c) Constant current testing of a fuel cell at 50 mA cm^{-2} for different catalysts. The experiments were performed under hydrogen flow rate of 15 mL min^{-1} at room temperature and atmospheric pressure. (d) The changes on normalized cell voltage of H-Pt NRs/C and commercial Pt/C before and after 72 h constant current discharge at 50 mA cm^{-2}.*

decreases and broadens, showing the absence of Van Hove singularities with short-range order (SRO) lost (Figures 5a–d). Driven from strong p–d coupling from good glass-forming Te, the overall Pt-distorted lattice reaches a meta-stable state, of which the total energetic trend undergoes a monotonic decrease and increased amorphization. Meanwhile, the active electronic orbitals lying near E_F are electron-rich with less site preference (Figure 5e). Taking the most preferred model (model 3), we observed the p–d electronic interplay of the initial oxygen adsorption performance. The lattice distortion-induced Pt-5d band center has already overlapped with the lone-pair state of O_2, guaranteeing significant electron transfer for adsorptions spreading within the dominant Pt-5d peak. This demonstrates strong and active electronegativity switching between locally distorted Pt sites and adsorbed O_2 (Figures 5f and 5g).

The 5d-electron–lattice coupling-induced optimal Pt-5d electronegativity switching via short-range disorder (SRDO) is now understood. The simulated RDF displays the degree of local disordering of Pt physically, where the dominant peak confirms the degree of

disordering, especially to the nearest Pt–Pt distance (Figure 5h). In contrast to the degree of disordering, the total energy anomaly decreases, while the Pt–Pt distance also decreases. Extraordinarily, the active 5d–5d Coulombic repulsion has increased the total energy. This arises because the strong SRDO enhances the electron–lattice coupling to vastly reduce Coulombic repulsion to attain more electronegativity in Pt-5d orbitals. Further study of the surface electronic work function confirms the contrast that the electronic activity increases followed by an increase of SRDO with support by on-site Pt-5d negative correlation energy (U_{eff}) among the distorted sites. It should be noted that such an on-site orbital correlation energy (U_{eff}) indicates an energy barrier for accepting two electrons at a same site, which overcomes the Coulombic repulsion and relaxes the Pauli spin-forbidden principle via strong lattice disorders (Figure 5i). We further demonstrated that the negative-U_{eff} ($-U_{eff}$) dominates the orbital electronegativity and drives the ORR catalysis by Pt with a strong SRDO. Following the conventional d-band center calculation, we determined that the Pt-5d center presents nearly the same level between the Pt-lattices with SRO and strongest SRDO character.
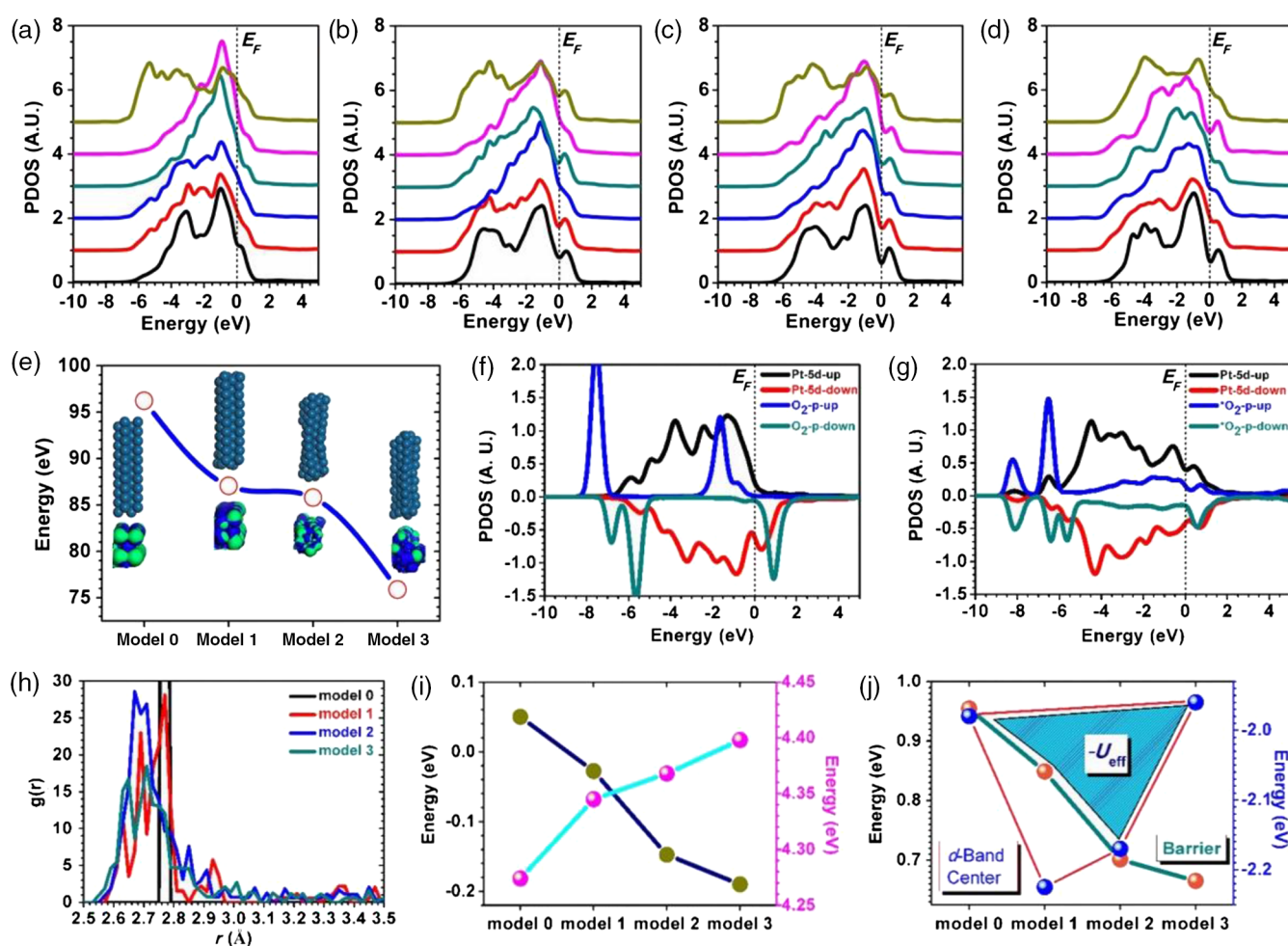
Figure 5 | *SRDO-dependent structural modeling and DFT calculations on electronic properties. (a–d) Site-dependent Pt-5d PDOSs of models 0, 1, 2, and 3, respectively. (e) Total energy variation related to models 0, 1, 2, and 3, respectively, with reference to the Pt–bulk metal. (f) PDOSs of Pt-5d and O_2-2p bands before initial O-adsorption during the ORR process. (g) PDOSs of Pt-5d and O_2-2p bands after stable O-adsorption. (h) Simulated RDF for models 0, 1, 2, and 3, respectively. (i) Effective Pt-5d orbital correlation energy (dark yellow point connected with dark blue line) and surface work functions (pink point connected with cyan line) for models 0, 1, 2, and 3, respectively. (j) ORR barrier related to models 0, 1, 2, and 3, respectively (orange point connected with green line) and their corresponding Pt-5d band centers (blue point connected with red line).*

Meanwhile, with an increased degree of SRDO, the Pt-5d band centers gradually reach higher levels toward E_F. This is attributed to the effective Pt-5d negative-U_{eff} under strong SRDO environment, which self-activates electronegativity and elevates the ORR efficiency with a minimized overall reaction barrier (Figure 5j). Further ORR pathway discussion confirms (Supporting Information Figure S17) that the local Pt lattice with strong SRDO can provide extra-active electron-transfer efficiency without a Coulombic repulsion barrier or negative trend, which accomplishes high electronic activities and ORR performance simultaneously.

To further explore the origin of much enhanced electrocatalytic performances for H-Pt NRs/C compared with W-Pt NRs/C and commercial Pt/C, X-ray photoelectron spectroscopy (XPS) was used to further analyze their electronic structures and chemical states (Supporting Information Figure S18). We found that the binding energy of Pt 4f for H-Pt NRs/C and W-Pt NRs/C (Supporting Information Figures S18a–d) was lower than that of commercial Pt/C (Supporting Information Figures S18e and f), showing the effectively modified electronic structures of H-Pt NRs/C and W-Pt NRs/C that mainly resulted from their distorted nanostructures. More significantly, the H-Pt NRs/C displays the highest fraction of Pt (II) (33.2%; Supporting Information Figures S18b, d, and f), indicating the largest degree of structural defects,[44-46] which is consistent with the maximized distortion (numerous facet boundaries, ubiquitous facets, general global strain, and so on) of these highly distorted Pt NRs. Consequently, the highly distorted

configuration mediates the activation, transmission, and desorption of O_2 located at free Pt sites and accelerates the kinetic process of O_2 reduction, resulting in the highest ORR activity of H-Pt NRs/C. Additionally, we analyzed the electronic structure and chemical state of H-Pt NRs/C after the ORR stability test. As shown in Supporting Information Figure 19, the binding energy of Pt 4f and a substantial fraction of Pt (II) (31.3%; Supporting Information Figure S19b) for H-Pt NRs/C can be well maintained after 30,000 potential cycles of ADTs, which endows the highly distorted Pt NRs with excellent ORR durability.

Conclusions

To conclude, we have developed a new class of high-efficiency Pt electrocatalysts to simultaneously boost the cathodic half reaction and overall reaction for PEMFCs. The H-Pt NRs have been created from the initially synthesized spongy $PtTe_2$ NRs through a series of sequential chemical and electrochemical aging processes. As demonstrated, the H-Pt NRs exhibit the highest activity toward ORR among these catalysts studied with specific and mass activities of 4.70 mA cm^{-2} and 2.77 A mg$^{-1}_{Pt}$ at 0.90 V versus RHE, respectively, which are 18.8 and 16.3 times higher than those of the commercial Pt/C. H-Pt NRs are also highly stable for ORR with negligible activity decay even after long-term 30,000 CV cycles. DFT calculations reveal that, in the realm of strong lattice distortion, electron–lattice coupling is significant for effective on-site electron transfer, which overcomes Coulombic repulsion and relaxes the Pauli spin-forbidden principle to reach extra-high electronegative reactivity for ORR. The unique H-Pt NRs also demonstrate much higher activity and lifetime for real fuel cells than the state-of-the-art commercial Pt/C, showing a novel class of advanced Pt nanocatalysts with both high activity and durability for fuel cell cathodic reactions. If there are other reactions, please note them.

Supporting Information

Supporting Information is available.

Conflicts of Interest

There are no conflicts to declare.

Author Contributions

X.Q.H. and L.Z.B. conceived and supervised the research. X.Q.H., L.Z.B., and Y.M.Z. designed the experiments, collected and analyzed the data. B.L.H. performed the DFT simulations. F.D.N. and X.C.Z. measured the MEA performances of different catalysts. X.Q.H. and L.Z.B. wrote the paper. All authors discussed the results and commented on the manuscript.

Acknowledgments

References

1. Tian, X. L.; Zhao, X.; Su, Y. Q.; Wang, L. J.; Wang, H. M.; Dang, D.; Chi, B.; Liu, H. F.; Hensen, E. J. M.; Lou, X. W.; Xia, B. Y. Engineering Bunched Pt–Ni Alloy Nanocages for Efficient Oxygen Reduction in Practical Fuel Cells. *Science* **2019**, *366*, 850–856.

2. Shao, M. H.; Chang, Q. W.; Dodelet, J. P.; Chenitz, R. Recent Advances in Electrocatalysts for Oxygen Reduction Reaction. *Chem. Rev.* **2016**, *116*, 3594–3657.

3. Yan, X. C.; Jia, Y.; Yao, X. D. Defects on Carbons for Electrocatalytic Oxygen Reduction. *Chem. Soc. Rev.* **2018**, *47*, 7628–7658.

4. Debe, M. K. Electrocatalyst Approaches and Challenges for Automotive Fuel Cells. *Nature* **2012**, *486*, 43–51.

5. Stamenkovic, V. R.; Fowler, B.; Mun, B. S.; Wang, G. F.; Ross, P. N.; Lucas, C. A.; Marković, N. M. Improved Oxygen Reduction Activity on Pt₃Ni (111) via Increased Surface Site Availability. *Science* **2007**, *315*, 493–497.

6. Wan, X.; Liu, X. F.; Li, Y. C.; Yu, R. H.; Zheng, L. R.; Yan, W. S.; Wang, H.; Xu, M.; Shui, J. L. Fe–N–C Electrocatalyst with Dense Active Sites and Efficient Mass Transport for High-Performance Proton Exchange Membrane Fuel Cells. *Nat. Catal.* **2019**, *2*, 259–268.

7. Chong, L. N.; Wen, J. G.; Kubal, J.; Sen, F. G.; Zou, J. X.; Greeley, J.; Chan, M.; Barkholtz, H.; Ding, W. J.; Liu, D. J. Ultralow-Loading Platinum–Cobalt Fuel Cell Catalysts Derived from Imidazolate Frameworks. *Science* **2018**, *362*, 1276–1281.

8. Liu, H. L.; Nosheen, F.; Wang, X. Noble Metal Alloy Complex Nanostructures: Controllable Synthesis and Their Electrochemical Property. *Chem. Soc. Rev.* **2015**, *44*, 3056–3078.

9. Wang, Y. J.; Zhao, N. N.; Fang, B. Z.; Li, H.; Bi, X. T. T.; Wang, H. J. Carbon-Supported Pt-Based Alloy Electrocatalysts for the Oxygen Reduction Reaction in Polymer Electrolyte Membrane Fuel Cells: Particle Size, Shape, and Composition Manipulation and Their Impact to Activity. *Chem. Rev.* **2015**, *115*, 3433–3467.

10. Bu, L. Z.; Zhang, N.; Guo, S. J.; Zhang, X.; Li, J.; Yao, J. L.; Wu, T.; Lu, G.; Ma, J. Y.; Su, D.; Huang, X. Q. Biaxially Strained PtPb/Pt Core/Shell Nanoplate Boosts Oxygen Reduction Catalysis. *Science* **2016**, *354*, 1410–1414.

11. Li, M. F.; Zhao, Z. P.; Cheng, T.; Fortunelli, A.; Chen, C. Y.; Yu, R.; Zhang, Q. H.; Gu, L.; Merinov, B. V.; Lin, Z. Y.; Zhu, E. B.; Yu, T.; Jia, Q. Y.; Guo, J. H.; Zhang, L.; Goddard III, W. A.; Huang, Y.; Duan, X. F. Ultrafine Zigzag Platinum Nanowires Enable High Platinum Mass Activity for the Oxygen Reduction Reaction. *Science* **2016**, *354*, 1414–1419.

12. Liu, M. L.; Zhao, Z. P.; Duan, X. F.; Huang, Y. Nanoscale Structure Design for High-Performance Pt-Based ORR Catalysts. *Adv. Mater.* **2019**, *31*, 1802234.

13. Gasteiger, H. A.; Kocha, S. S.; Sompalli, B.; Wagner, F. T. Activity Benchmarks and Requirements for Pt, Pt-Alloy, and Non-Pt Oxygen Reduction Catalysts for PEMFCs. *Appl. Catal. B: Environ.* **2005**, *56*, 9–35.

14. Gasteiger, H. A.; Marković, N. M. Just a Dream-or Future Reality? *Science* **2009**, *324*, 48–49.

15. Bing, Y. H.; Liu, H. S.; Zhang, L.; Ghosh, D.; Zhang, J. J. Nanostructured Pt-Alloy Electrocatalysts for PEM Fuel Cell Oxygen Reduction Reaction. *Chem. Soc. Rev.* **2010**, *39*, 2184–2202.

16. Mao, J. J.; Chen, W. X.; He, D. S.; Wan, J. W.; Pei, J. J.; Dong, J. C.; Wang, Y.; An, P. F.; Jin, Z.; Xing, W.; Tang, H. L.; Zhuang, Z. B.; Liang, X.; Huang, Y.; Zhou, G.; Wang, L. Y.; Wang, D. S.; Li, Y. D. Design of Ultrathin Pt–Mo–Ni Nanowire Catalysts for Ethanol Electrooxidation. *Sci. Adv.* **2017**, *3*, e1603068.

17. Chen, C.; Kang, Y. J.; Huo, Z. Y.; Zhu, Z. W.; Huang, W. Y.; Xin, H. L.; Snyder, J. D.; Li, D. G.; Herron, J. A.; Mavrikakis, M.; Chi, M. F.; More, K. L.; Li, Y. D.; Markovic, N. M.; Somorjai, G. A.; Yang, P. D.; Stamenkovic, V. R. Highly Crystalline Multimetallic Nanoframes with Three-Dimensional Electrocatalytic Surfaces. *Science* **2014**, *343*, 1339–1343.

18. Huang, X. Q.; Zhao, Z. P.; Cao, L.; Chen, Y.; Zhu, E. B.; Lin, Z. Y.; Li, M. F.; Yan, A. M.; Zettl, A.; Wang, Y. M.; Duan, X. F.; Mueller, T.; Huang, Y. High-Performance Transition Metal-Doped Pt₃Ni Octahedra for Oxygen Reduction Reaction. *Science* **2015**, *348*, 1230–1234.

19. He, D. P.; Zhang, L. B.; He, D. S.; Zhou, G.; Lin, Y.; Deng, Z. X.; Hong, X.; Wu, Y. E.; Chen, C.; Li, Y. D. Amorphous Nickel Boride Membrane on a Platinum–Nickel Alloy Surface for Enhanced Oxygen Reduction Reaction. *Nat. Commun.* **2016**, *7*, 12362.

20. Lim, B.; Jiang, M. J.; Camargo, P. H. C.; Cho, E. C.; Tao, J.; Lu, X. M.; Zhu, Y. M.; Xia, Y. N. Pd-Pt Bimetallic Nanodendrites with High Activity for Oxygen Reduction. *Science* **2009**, *324*, 1302–1305.

21. van der Vliet, D. F.; Wang, C.; Tripkovic, D.; Strmcnik, D.; Zhang, X. F.; Debe, M. K.; Atanasoski, R. T.; Markovic, N. M.; Stamenkovic, V. R. Mesostructured Thin Films as Electrocatalysts with Tunable Composition and Surface Morphology. *Nat. Mater.* **2012**, *11*, 1051–1058.

22. Li, H. H.; Zhao, S.; Gong, M.; Cui, C. H.; He, D.; Liang, H. W.; Wu, L.; Yu, S. H. Ultrathin PtPdTe Nanowires as Superior Catalysts for Methanol Electrooxidation. *Angew. Chem. Int. Ed.* **2013**, *52*, 7472–7476.

23. Cui, C. H.; Gan, L.; Heggen, M.; Rudi, S.; Strasser, P. Compositional Segregation in Shaped Pt Alloy Nanoparticles and Their Structural Behaviour During Electrocatalysis. *Nat. Mater.* **2013**, *12*, 765–771.

24. Chattot, R.; Bacq, O. L.; Beermann, V.; Kühl, S.; Herranz, J.; Henning, S.; Kühn, L.; Asset, T.; Guétaz, L.; Renou, G.; Drnec, J.; Bordet, P.; Pasturel, A.; Eychmüller, A.; Schmidt, T. J.; Strasser, P.; Dubau, L.; Maillard, F. Surface Distortion as a Unifying Concept and Descriptor in Oxygen Reduction Reaction Electrocatalysis. *Nat. Mater.* **2018**, *17*, 827–833.

25. Stamenkovic, V. R.; Mun, B. S.; Arenz, M.; Mayrhofer, K. J. J.; Lucas, C. A.; Wang, G. F.; Ross, P. N.; Markovic, N. M. Trends in Electrocatalysis on Extended and Nanoscale Pt-Bimetallic Alloy Surfaces. *Nat. Mater.* **2007**, *6*, 241–247.

26. Strasser, P.; Koh, S.; Anniyev, T.; Greeley, J.; More, K.; Yu, C. F.; Liu, Z. C.; Kaya, S.; Nordlund, D.; Ogasawara, H.; Toney, M. F.; Nilsson, A. Lattice-Strain Control of the Activity in Dealloyed Core-Shell Fuel Cell Catalysts. *Nat. Chem.* **2010**, *2*, 454–460.

27. Zhang, S.; Zhang, X.; Jiang, G. M.; Zhu, H. Y.; Guo, S. J.; Su, D.; Lu, G.; Sun, S. H. Tuning Nanoparticle Structure and Surface Strain for Catalysis Optimization. *J. Am. Chem. Soc.* **2014**, *136*, 7734–7739.

28. Clark, S. J.; Segall, M. D.; Pickard, C. J.; Hasnip, P. J.; Probert, M. I. J.; Refson, K.; Payne, M. C. First Principles Methods Using CASTEP. *Z. Kristallogr.* **2005**, *220*, 567–570.

29. Anisimov, V. I.; Aryasetiawan, F.; Lichtenstein, A. I. First-Principles Calculations of the Electronic Structure and Spectra of Strongly Correlated Systems: the LDA + U Method. *J. Phys. Condens. Matter* **1997**, *9*, 767–808.

30. Huang, B. L.; Gillen, R.; Robertson, J. Study of CeO₂ and its Native Defects by Density Functional Theory with Repulsive Potential. *J. Phys. Chem. C* **2014**, *118*, 24248–24256.

31. Huang, B. L. Superiority of DFT + U with Non-Linear Core Correction for Open-Shell Binary Rare-Earth Metal Oxides: A Case Study of Native Point Defects in Cerium Oxides. *Philos. Mag.* **2014**, *94*, 3052–3071.

32. Huang, B. L. 4f Fine-Structure Levels as the Dominant Error in the Electronic Structures of Binary Lanthanide Oxides. *J. Comput. Chem.* **2016**, *37*, 825–835.

33. Huang, B. L. Intrinsic Deep Hole Trap Levels in Cu₂O with Self-Consistent Repulsive Coulomb Energy. *Solid State Commun.* **2016**, *230*, 49–53.

34. Huang, B. L. Strong Compensation Hinders the p-Type Doping of ZnO: a Glance Over Surface Defect Levels. *Solid State Commun.* **2016**, *237–238*, 34–37.

35. Huang, B. L. Unraveling Energy Conversion Modeling in the Intrinsic Persistent Upconverted Luminescence of Solids: A Study of Native Point Defects in Antiferromagnetic Er₂O₃. *Phys. Chem. Chem. Phys.* **2016**, *18*, 13564–13582.

36. Marzari, N.; Vanderbilt, D.; Payne, M. C. Ensemble Density-Functional Theory for Ab Initio Molecular Dynamics of Metals and Finite-Temperature Insulators. *Phys. Rev. Lett.* **1997**, *79*, 1337–1340.

37. Probert, M. I. J.; Payne, M. C. Improving the Convergence of Defect Calculations in Supercells: an ab Initio Study of

the Neutral Silicon Vacancy. *Phys. Rev. B* **2003**, *67*, 075204.

38. Kleinman, L.; Bylander, D. M. Efficacious Form for Model Pseudopotentials. *Phys. Rev. Lett.* **1982**, *48*, 1425–1428.

39. Louie, S. G.; Froyen, S.; Cohen, M. L. Nonlinear Ionic Pseudopotentials in Spin-Density-Functional Calculations. *Phys. Rev. B* **1982**, *26*, 1738–1742.

40. Grinberg, I.; Ramer, N. J.; Rappe, A. M. Transferable Relativistic Dirac-Slater Pseudopotentials. *Phys. Rev. B* **2000**, *62*, 2311–2314.

41. Rappe, A. M.; Rabe, K. M.; Kaxiras, E.; Joannopoulos, J. D. Optimized Pseudopotentials. *Phys. Rev. B* **1990**, *41*, 1227–1230.

42. Huang, B. L. The Screened Pseudo-Charge Repulsive Potential in Perturbed Orbitals for Band Calculations by DFT + U. *Phys. Chem. Chem. Phys.* **2017**, *19*, 8008–8025.

43. U.S. Department of Energy, Technical Plan: Fuel Cells, **2016**. (http://www.energy.gov/sites/prod/files/2016/06/f32/fcto_myrdd_fuel_cells_0.pdf).

44. Blume, R.; Niehus, H.; Conrad, H.; Böttcher, A. Surface-Defect-Mediated Channel for Oxygen Incorporation into Ru (0001). *J. Phys. Chem. B* **2004**, *108*, 14332–14339.

45. Sun, X. H.; Jiang, K. Z.; Zhang, N.; Guo, S. J.; Huang, X. Q. Crystalline Control of {111} Bounded Pt_3Cu Nanocrystals: Multiply-Twinned Pt_3Cu Icosahedra with Enhanced Electrocatalytic Properties. *ACS Nano* **2015**, *9*, 7634–7640.

46. Zhang, J. W.; Ye, J. Y.; Fan, Q. Y.; Jiang, Y. T.; Zhu, Y. F.; Li, H. Q.; Cao, Z. M.; Kuang, Q.; Cheng, J.; Zheng, J.; Xie, Z. X. Cyclic Penta-Twinned Rhodium Nanobranches as Superior Catalysts for Ethanol Electro-Oxidation. *J. Am. Chem. Soc.* **2018**, *140*, 11232–11240.